Generation of picosecond ion pulses using laser-stimulated desorption from a tungsten nanotip

Alexander Redl [1,*] Markus Goldberger [1] Christoph Pachlinger,[1] Franz I. Pfanner [2] and Richard A. Wilhelm [1,†]
[1] *TU Wien, Institute of Applied Physics, 1040 Vienna, Austria*
[2] *California Institute of Technology, Pasadena, California 91125, USA*

(Received 8 September 2025; accepted 24 November 2025; published 19 December 2025)

We present an experimental approach to the formation of sub-100 ps ion pulses at 4.5−8.5 keV energies using laser-stimulated desorption from a tungsten nanotip at room temperature. The illumination of the tip apex with femtosecond ultraviolet laser pulses results in the ionization of adsorbed atomic and molecular species through the enhancement of a localized electric field. Unlike photoionization of atoms and molecules in the gas phase in extended volumes, determined by a typical laser focal volume, our approach naturally exploits a nanometric ionization region from tungsten nanotips with tip radii of 15−150 nm and operates at a moderate optical fluence of 10^{11} W/cm^2. Time-of-flight measurements demonstrate stable and well-timed ion pulses. A systematic exploration of the ion pulse characteristics on laser parameters and loading gas pressures has been conducted. Our compact, yet simple, source design renders time-resolved ion-solid interaction studies practically possible, paving the way for future pump-probe studies.

DOI: 10.1103/7wdx-97pf

I. INTRODUCTION

The interaction of ions with solids is governed by a complex interplay between many-body electronic and nuclear interactions on a broad range of timescales from femto- to nanoseconds. This complexity, manifesting across multiple levels, limits the ability to truly predict industrially significant processes such as surface atom sputtering, layer intermixing, and damage formation, despite decades of extensive research [1–5]. Whilst modern molecular dynamics simulations are capable of elucidating certain interaction processes, the reliability of such simulations [6,7] strongly depends on the choice of interaction potentials. Direct testing of the simulated picosecond dynamics subsequent to an ion impact remains unfeasible in experimental settings.

Implementing an ion-based pump-probe experimental scheme further demands synchronization of a probing laser pulse with the ion-impact-excitation of a surface [8–10]. Although established methods enable the generation of electron pulses with subpicosecond durations [11,12], achieving comparable temporal resolution for ions remains a challenge due to their greater mass and momentum spread [13]. Proton pulses with a duration of 3.5 ps at MeV energies were demonstrated [14], and 18 ps Ne^+ pulses were achieved in the keV regime [15,16]. However, these methods require high optical laser powers exceeding 10^{15} W/cm^2, typically employed for direct photoionization within ion-buncher configurations and with cooled gas jets. Additionally, electrostatic choppers have been shown to produce 295 ps He^+ pulses from a continuous ion beam (as measured without correction for detector broadening). Timely synchronization with another pulse for a pump-probe scheme has not yet been experimentally realized [17]. An alternative approach involves ultrashort electron pulses to induce electron-stimulated desorption, thereby generating short ion pulses at keV energies [18]. This technique benefits from the precise spatial definition of the ionization region at a solid surface, which is a key to producing picosecond ion pulses in general.

Laser-induced desorption and ablation are well-characterized phenomena. Both rely on pulsed laser excitation to eject atoms, ions, or molecules from a solid surface. Whereas ablation removes bulk material and alters the substrate, desorption proceeds without detectable changes to the surface composition or morphology [19]. In contrast, atom probe tomography (APT) is based on laser-assisted field evaporation from a nanotip apex, where a strong electric field drives the removal of surface atoms as ions [20]. Unlike desorption, APT is inherently destructive since the specimen is progressively consumed during analysis. Ultrafast timing resolution is typically nonessential as long as the extracted ionic species can be well identified by their time of flight (TOF). Laser-induced desorption, by comparison, remains an established spectroscopy technique valued for its nondestructive interaction allowing for long-term stable operation [21,22].

Sharp metallic tips provide localized electric fields at their apex and are widely used to explore strong-field phenomena such as laser-induced field emission of electrons [23–25]. The strong field enhancement and nanometric emission area make such nanotips ideal platforms for studying ultrafast photoemission and desorption dynamics. These characteristics motivate their use here for generating picosecond ion pulses through laser-stimulated desorption.

*Contact author: redl@iap.tuwien.ac.at
†Contact author: wilhelm@iap.tuwien.ac.at

Published by the American Physical Society under the terms of the Creative Commons Attribution 4.0 International license. Further distribution of this work must maintain attribution to the author(s) and the published article's title, journal citation, and DOI.

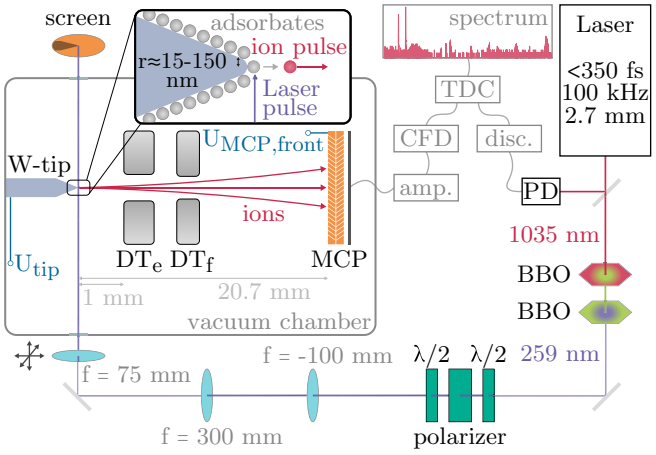


FIG. 1. Schematic of the pulsed ion source utilizing laser-stimulated desorption. A UV laser pulse is focused onto a tungsten nanotip, ionizing adsorbates. The generated ions are extracted and focused by drift tubes (DT_e and DT_f) onto the microchannel plate (MCP) detection system. A time-of-flight spectrum is subsequently constructed by timing each MCP signal relative to the preceding laser pulse.

In this work, we show how the concept of laser induced desorption can be extended toward nanometric tips as ion emitters. We present experimental results of ultrashort ion pulse formation for different ion masses and discuss the underlying processes of this class of ion sources for time-resolved studies. We systematically investigate how ion pulse width and ion yield depend on various experimental parameters, including laser pulse energy, repetition rate, polarization, gas pressure, and electrode potentials.

II. METHODS

A. Experimental setup

Our ion source, schematically illustrated in Fig. 1, consists of an electrochemically etched tungsten nanotip, fabricated in-house from a tungsten wire with an initial diameter of 0.5 mm. An etching solution of potassium hydroxide (KOH) was used [26]. Scanning electron microscopy (SEM) analysis determined that the etched tip radii for different tips were in the range of 15–150 nm, with a cone half-angle of approximately 10° in the apex region. The nanotip is placed within a vacuum chamber, biased to a positive high potential, and irradiated with a UV laser of 259 nm wavelength in a pulsed fashion.

The UV laser is derived from a pulsed infrared (IR) laser beam at a wavelength of 1035 nm, originating from a Coherent Monaco 1035-40-40 laser system [27]. The initial IR beam has a diameter of 2.7 mm ($1/e^2$) and <350 fs pulse duration. The laser system enables control of pulse energy and repetition rate. Frequency conversion to the UV range is 108 achieved through two successive second-harmonic generation 2 109 stages utilizing β-barium borate (BBO) nonlinear crystals [28].

Passing the resulting UV laser through a half-wave plate ($\lambda/2$) and a polarizer allows precise control of the laser power. A following additional $\lambda/2$ plate allows free adjustment of the linear laser polarization.

After expansion, the beam is focused onto the apex of the tungsten nanotip using a movable lens with a focal length of 75 mm, achieving a calculated full-width-at-half-maximum (FWHM) spot size of approximately 3.6 μm. The UV laser pulse energy ranges between 5 and 12 nJ, corresponding to optical intensities of $2.0–4.5 \times 10^{11}$ W/cm^2. This results in an energy density per pulse of approximately 0.1–0.2 J/cm^2.

The precise positioning of the UV laser on the nanotip apex is achieved by monitoring the transmitted laser beam on a fluorescent screen after it has been focused onto the tip (cf. Fig. 1). The presence of the tip casts a shadow on the screen, allowing for accurate alignment. Fine adjustments to the laser position are made by translating the movable focusing lens, which is mounted on a three-axis translation stage.

A needle valve is used to introduce a controlled amount of various working gases into the vacuum chamber, generally maintaining a partial gas pressure in the range of 1×10^{-8} to 5×10^{-5} mbar, with a base pressure $<1 \times 10^{-9}$ mbar between consecutive experiments. The choice of gas determines the ion species generated by the system, as the gas molecules adsorb onto the surface of the tungsten nanotip at room temperature. When the nanotip is irradiated by the UV laser pulse, ionization occurs via laser-stimulated desorption and the subsequent emission of these ions from the tip. Therefore, a pulsed ion beam is generated, which is correlated in time to the initial laser pulse.

An extraction drift tube (DT_e), positioned 1 mm in front of the tungsten nanotip, generates a strong electric field (∼65 MV/cm) in the vicinity of the tip to accelerate ions, but below the field ionization threshold. A second drift tube (DT_f), located 2 mm from DT_e, focuses the ion beam while simultaneously forming an aperture to limit the maximal divergence of emitted ions. DT_e is 3.5 mm thick with an inner diameter of 3.2 mm, whereas DT_f is 1 mm thick with a 2 mm inner diameter. This geometry ensures that only ions with similar paths are transmitted to the detector, consequently reducing the temporal spread of the ion beam at the detector. Following the drift tube assembly, the ions travel toward the front plate of an MCP detector. The detector is positioned 20.7 mm from the tip and is biased to a potential of −1.95 kV. This voltage is selected to optimize detector signal quality, as the back side of the MCP is on ground potential, and this voltage across the MCP in Chevron-stack configuration provides the best detector response. The typical operating potentials for the system components are $U_{tip} = +6500$ V, $U_{DT_e} = -1850$ V, $U_{DT_f} = -1850$ V, and $U_{MCP,\,front} = -1950$ V. With these potentials, the singly charged ions thus reach the detector with a kinetic energy of 8.45 keV.

Time stamping of ions is performed using the MCP detector in coincidence with a fixed trigger signal obtained by a photodiode (PD; Femto HSPR-X-I-2G-IN), which triggers on a portion of the initial IR laser pulse. Data acquisition starts when part of the IR laser pulse is detected by the PD and converted into an analog signal. The signal is then processed by a pico-timing discriminator (disc; ORTEC 9307), which converts it into a fast nuclear instrumentation module (NIM) pulse serving as the start signal for a time-to-digital converter (TDC; RoentDek TDC8HP). When ions impact the MCP

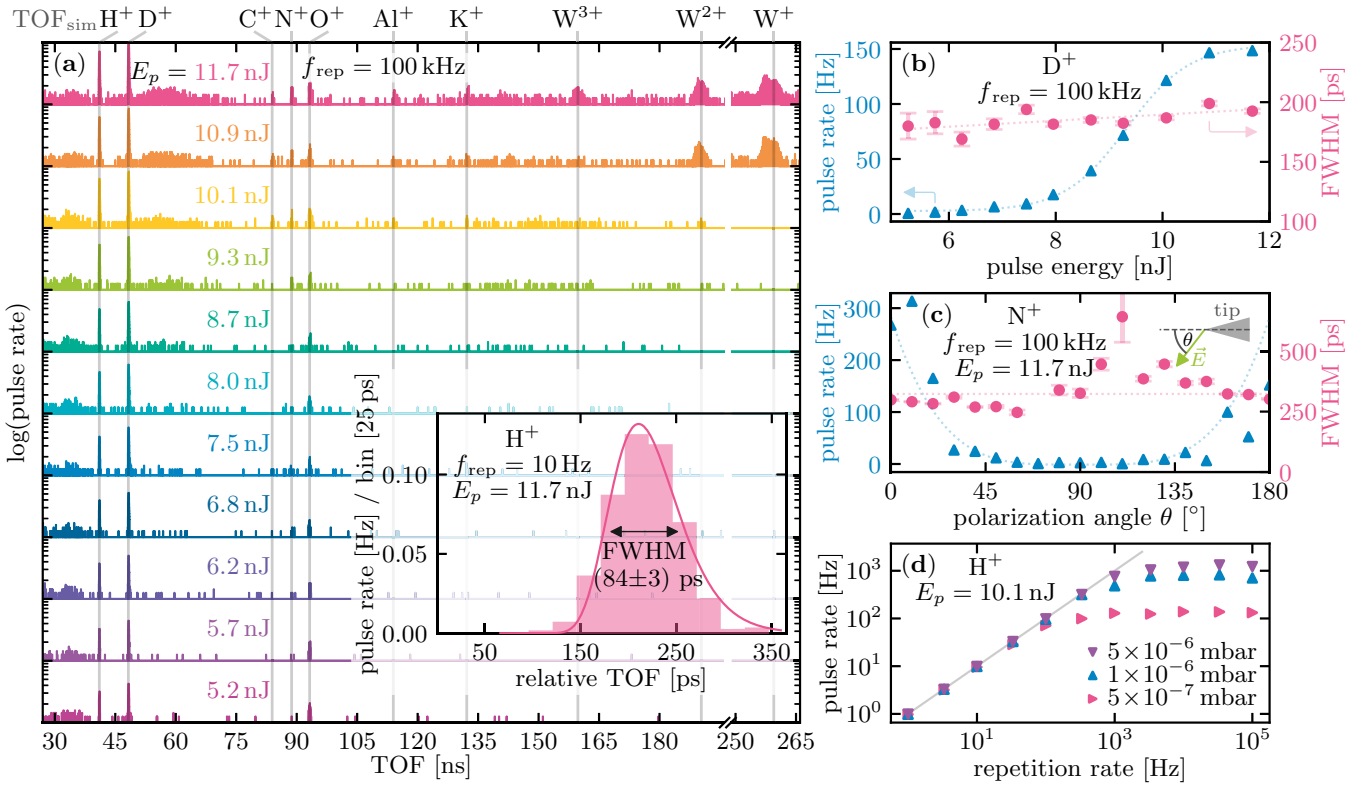


FIG. 2. (a) Ion TOF spectra recorded at various laser pulse energies E_p vertically offset for clarity, at a fixed laser repetition rate f_{rep} of 100 kHz. Gray vertical lines indicate simulated TOF values for different ion species, based on SIMION simulations. The inset plot shows an average hydrogen ion peak, featuring a peak width (FWHM) of 84 ± 3 ps. (b) Dependence of deuterium ion pulse width and MCP pulse rate on laser pulse energy at fixed f_{rep}. (c) Laser polarization-dependent MCP pulse rate and pulse width of nitrogen ions for fixed laser repetition rate and pulse energy. (d) MCP pulse rate of hydrogen ions as a function of laser repetition rate for different hydrogen partial pressures, at fixed laser pulse energy.

detector, they generate an analog signal with an approximately 100 V dc offset (anode bias). This signal is first passed through an ac signal decoupler (RoentDek HFSD-SMA-SHV 10 kΩ) to remove the dc component and then amplified by 40 dB using a 2 GHz amplifier (amp.; Femto HSA-Y-2-40). Due to the variable amplitude of MCP signals, a constant-fraction discriminator (CFD; RoentDek CFD1x) processes the signal, generating an NIM output that acts as the stop signal for the TDC. The average bin size is specified as ∼25 ps and limits the precision of ion peak width determination, particularly at low count rates. In addition to ion detection, stray laser reflections from the tungsten tip produce signals on the MCP, which are also analyzed by the electronics. Each ion's TOF is determined by computing the difference between the PD trigger signal and the corresponding MCP ion signal. To correct for systematic timing offsets, this value is further adjusted by subtracting the average time difference between the PD signal and the laser reflection signal on the MCP. Note that the ion pulse width here is the result of the TOF measurement of laser-to-ion pulses and reflects therefore the ion arrival time distribution for cases of $\lesssim 1$ ion per pulse and not necessarily the individual pulse widths for cases of $\gg 1$ ions per pulse.

B. Ion trajectory simulations

To complement our experimental results, charged particle trajectory simulations were performed using the SIMION software package [29]. The electrostatic field surrounding the tungsten nanotip and the propagation of ions from tip apex to the MCP detector were modeled using the experimentally implemented electrode geometry and potentials. Ions were initialized at the apex of the nanotip and propagated through the simulated field to yield TOF distributions for different ion species and charge states.

The simulation grid resolution was set to 0.05 mm, which provides a balance between computational feasibility and sufficient accuracy for reproducing TOF peak positions for different charge-mass ratios over the 20.7 mm ion flight path.

III. RESULTS

A set of TOF spectra is presented in Fig. 2(a), acquired at a fixed laser repetition rate (f_{rep}) of 100 kHz, and the vacuum chamber filled with deuterium gas at a partial pressure of 5×10^{-7} mbar. Each individual spectrum corresponds to a different laser pulse energy (E_p), varied between 5.2 and 11.7 nJ, and is vertically offset for clarity. Distinct peaks appear at characteristic TOF values, corresponding to different ion species arriving at the MCP detector with mass- and charge-dependent flight times. To identify the ion species associated with each peak, charged particle trajectory simulations were performed using simion. The simulated ion species and charge state are labeled at the top of Fig. 2(a), while the

resulting simulated TOF values are marked as vertical gray lines. Experimental and simulation data show good agreement for all ion masses.

The inset displays a typical proton TOF peak at a reduced repetition rate of 10 Hz and a pulse energy of 11.7 nJ. The peak follows a lognormal distribution, reflecting a skewed Gaussian shape due to a lower TOF bound for any given mass being imposed by the shortest possible ion trajectory. Each ion pulse is characterized by its MCP pulse rate, mean TOF, and temporal ion pulse width. The latter is defined as the arrival time jitter and quantified by its FWHM. In the inset, the peak is fitted to extract the temporal resolution, which yields a pulse width of 84 ± 3 ps, with the uncertainty determined from the fit.

Focusing only on the deuterium ion peak in Fig. 2(b), an increase in MCP pulse rate with increasing laser pulse energy can be observed, while the ion pulse width remains largely unchanged. This suggests that higher laser pulse energies are advantageous for higher ion beam intensities without compromising peak resolution.

All measurements discussed this far were conducted with the laser polarization aligned along the axis of the nanotip, such that the electric field vector of the laser was parallel to the tip's symmetry axis, corresponding to a polarization angle θ of 0° [cf. Fig. 2(c)]. Under this configuration, the MCP pulse rate is maximized. When the laser polarization is rotated away from this alignment, the pulse rate decreases, reaching a minimum when the electric field of the laser is orthogonal to the tip axis. In Fig. 2(c), nitrogen ions were studied at a partial pressure of 5×10^{-6} mbar, a laser repetition rate of 100 kHz, and laser pulse energy of 11.7 nJ. Due to lower count rates at nonaligned polarization angles, the uncertainty in determining ion pulse widths increases.

Finally, Fig. 2(d) presents the dependence of effects of the MCP pulse rate on the laser repetition rate for protons. Here, the laser pulse energy was fixed at 10.1 nJ, and the partial pressure of hydrogen was varied from 5×10^{-7} to 5×10^{-6} mbar. Below a pressure-dependent threshold repetition rate, the MCP pulse rate follows the laser repetition rate, indicating that each laser pulse triggers corresponding ionization events and thus an MCP pulse. Above this threshold, the MCP pulse rate saturates at a value proportional to the hydrogen partial pressure. The gray diagonal line acts as an upper limit for MCP pulses, as it represents the laser repetition rate, which cannot be surpassed by the hydrogen pulse rate.

The influence of different gas species at varying partial pressures within the vacuum chamber is summarized in Fig. 3. The figure displays element-specific sections of the TOF histogram. The gray vertical lines indicate the elemental TOFs obtained from SIMION trajectory calculations. For each mass, individual measurements were performed at multiple partial pressures, with spectra vertically offset for clarity.

For deuterium and nitrogen, clear ion peaks are observed in the MCP signal, and the inset in Fig. 3 shows the integrated MCP pulse counts as a function of partial pressure. In both cases, the ion count rate increases linearly with gas pressure, indicating a direct proportionality between the number of desorbed ions and the available adsorbate coverage at the tip surface. All measurements were performed at a fixed laser repetition rate of 100 kHz and pulse energy of 11.7 nJ.

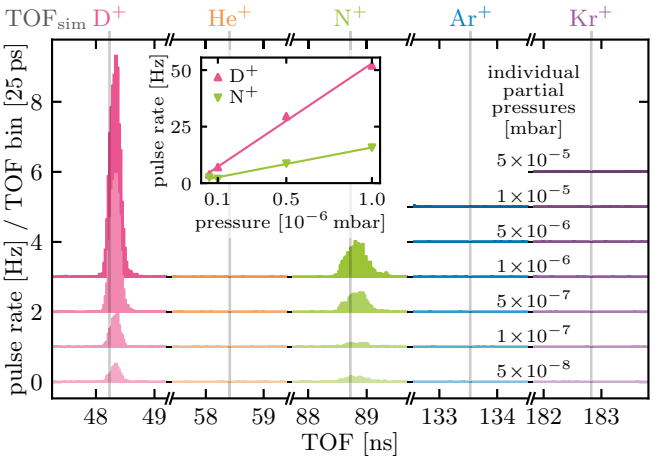


FIG. 3. TOF spectra of various ion species recorded at different partial pressures. The expected TOF values for each species, simulated using SIMION, are indicated by vertical gray lines and labeled at the top of the plot. Additionally, each element is represented by a distinct color and spectra at different partial pressures are vertically offset for clarity. The inset plot shows the total ion counts as a function of partial pressure for selected ion species.

In contrast, no clear ion-related features above background noise were observed for the investigated noble gases (helium, argon, and krypton), regardless of the applied partial pressure. This suggests that under the given experimental conditions at room temperature, these gases do not adsorb on the tip as expected from Refs. [30,31].

Varying the applied electrode potentials alters the trajectories of ions traveling from the nanotip to the detector, thereby affecting both the position and shape of the resulting ion peaks. This behavior is illustrated in Fig. 4, where all measurements were performed at a fixed laser repetition rate of 100 kHz and pulse energy of 11.7 nJ.

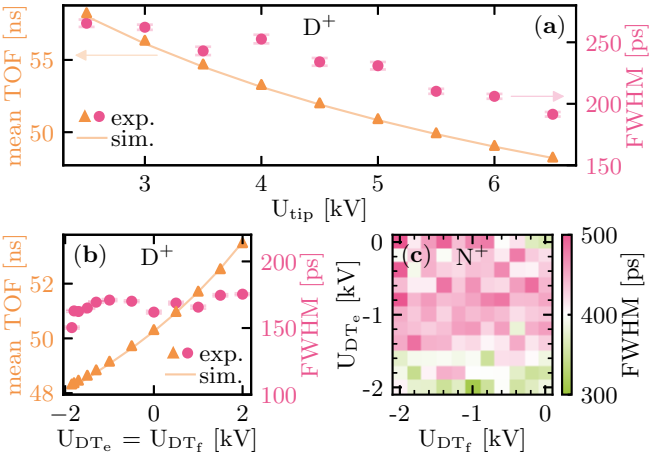


FIG. 4. Potential-dependent ion peak width and mean TOF. (a) Effect of varying the tungsten nanotip potential U_{tip} on the experimental and simulated TOF spectra of deuterium ions. (b) Variation of extraction drift tube DT_e and focusing DT_f potential. (c) Nitrogen ion peak width as a function of U_{DT_e} and U_{DT_f}.

In Fig. 4(a), the potential applied to the tungsten nanotip was varied while both DTs were held constant at −1850 V, with deuterium gas introduced at a partial pressure of 5×10^{-7} mbar. As the tip potential increases, the mean TOF of deuterium ions decreases, reflecting the corresponding increase in their kinetic energy, in excellent agreement with SIMION simulations. In addition, the ion peak narrows with higher tip potential, resulting in a reduced peak width.

Figure 4(b) shows the effect of varying both DT potentials equally, while the tip potential was held fixed at +6500 V. For deuterium ions, both experimental and simulation data confirm that lower DT potentials result in shorter mean TOF values, while the pulse width remains unaffected. The gas pressure and laser conditions were identical to those used in Fig. 4(a), for direct comparison.

In Fig. 4(c), the electrostatic potential of extraction and focusing DTs were varied independently for nitrogen ions, using a nitrogen partial pressure of 5×10^{-6} mbar, laser repetition rate of 100 Hz, and laser pulse energy of 10.9 nJ. While adjusting the focusing DT_f has little to no effect on the ion peak width, reducing the extraction DT_e potential leads to a noticeable narrowing of the peak.

IV. DISCUSSION

All detected ion species are presented in Fig. 2(a) and correspond to elements present within the experimental setup. Residual gases such as hydrogen, carbon, nitrogen, and oxygen are commonly found in high-vacuum environments. This happens particularly in the absence of chamber bake-out, as in our setup. The presence of potassium is attributed to remnants from the KOH etching solution used during the tungsten nanotip fabrication. Aluminum is traced to the conductive epoxy used for mounting the tip, as confirmed by energy-dispersive x-ray spectroscopy (EDX) analysis of both the epoxy and the tungsten nanotip itself. Tungsten ions, originating from direct laser-induced ablation of the tip, appear only at pulse energies exceeding 10 nJ. Given the laser focus spot size of 3.6 µm (FWHM), this corresponds to an energy density per pulse of approximately $0.1\,\mathrm{J/cm^2}$. Reported tungsten ablation thresholds range from ∼0.23 to $0.5\,\mathrm{J/cm^2}$ for 800 nm and 1030 nm laser pulses with durations between 15 fs and ∼40 ps [32–36] and ∼0.1 and $0.25\,\mathrm{J/cm^2}$ for 515 nm picosecond laser pulses [36]. Previous studies also indicate that the ablation threshold decreases for consecutive laser pulses [36]. Consequently, our estimated energy density of $0.1\,\mathrm{J/cm^2}$ likely represents the lower limit for tungsten ablation under the present laser conditions.

The mentioned ion species are present in all recorded TOF spectra. For Fig. 2(a), deuterium was intentionally introduced to the chamber to confirm the appearance of a corresponding ion peak in the TOF spectrum. In the absence of deuterium, the D^+ ion peak is not observed and therefore cannot be mistaken for $H_2{}^+$. The same applies to the N^+ ion peak, whose detector count increases linearly with increasing nitrogen partial gas pressure (cf. Fig. 3). This indicates that it does not originate from hydrocarbon fragments, as they would be independent of the nitrogen partial gas pressure.

Also, no evidence of multi-ionization during laser-stimulated desorption was found in any of the experiments. All investigated adsorbates, including hydrogen, deuterium, carbon, nitrogen, and oxygen, produced only singly charged ion peaks. The only multi-ionized element observed was tungsten, yielding W^{2+} and W^{3+} ions, which appear exclusively at high laser pulse energies and are attributed to laser ablation rather than desorption.

All experimentally determined ion peak widths ($\mathrm{FWHM_{exp}}$) are derived directly from raw TOF data, reflecting a convolution of the intrinsic ion arrival time distribution and the temporal jitter of the detection system. This system jitter consists of the MCP detector response and timing jitter in the electronics. We estimated the system response ($\mathrm{FWHM_{sys}}$) by directing the pulsed UV laser beam directly onto the MCP detector, relying on the assumption that the laser pulse duration of <350 fs is negligible compared to the system jitter. This approach yields a system response width of ≈100−150 ps. This system response width is slightly broader than some of the observed ion TOF peaks due to amplitude-dependent timing variations in the discriminator threshold. We therefore estimate a lower bound for the achievable temporal resolution of our setup to be ∼80−150 ps, depending on the MCP signal amplitude (i.e., particles or photons detected). Assuming both the intrinsic ion arrival distribution and the system jitter follow Gaussian profiles, their FWHMs add in quadrature. The intrinsic ion pulse width can therefore be estimated by $\mathrm{FWHM_{ion}} = \sqrt{\mathrm{FWHM_{exp}^2} - \mathrm{FWHM_{sys}^2}}$.

This lets us expect significantly shorter ion pulses, as reported above. However, we have chosen not to apply a correction to our analysis, because MCP signals for laser light and ions differ substantially in amplitude. This introduces systematic uncertainties for the timing electronics due to varying discrimination thresholds. The measured ion pulse width of 84 ps [cf. inset of Fig. 2(a)] is therefore not limited by the intrinsic desorption dynamics, but rather by the spatial dispersion of ion trajectories and the temporal resolution of the detection system. Ions emitted from slightly different positions on the tip surface experience marginally different flight paths, resulting in temporal broadening.

The observed ion emission is consistent with laser-induced desorption of adsorbed gas molecules [19], which depends on material-specific properties, as well as laser wavelength, polarization, power, and pulse duration. Furthermore, UV illumination enhances the local electric field at the nanotip apex, since the laser peak power density of $10^{11}\,\mathrm{W/cm^2}$ corresponds to ∼10 MV/cm. Given the nanometric confinement of the ionization volume, the initial ion spatial spread is expected to be minimal. However, the resulting ion energy distribution is influenced by both thermal excitation and variations in the desorption process. The thermal component is expected to be small due to the low CW-equivalent laser power. Although we do not directly measure the energy spread, the narrow pulse widths suggest a modest spread. Previous work using a 337 nm laser system with 300 ps pulses reported energy spreads of 2.1 eV for N_2 and 1.05 eV for D_2 [37] desorption. With these values in the simplified SIMION simulation, the resulting pulse widths would result in 23.8 ps for D_2 and 84.8 ps for N_2 ions.

For a nanotip with an apex radius of 150 nm and a height of 0.5 mm, the field enhancement factor is $\gamma \approx 700-900$ [38].

Applying a potential of +6500 V to the tungsten tip thus produces a local electric field of ∼65 MV/cm at the apex. Ablation of the tip throughout the measurements is indicated by the detection of tungsten ions. SEM analysis verifies that the tip was blunted in this case to a radius of 1250 nm, leading to a reduced field enhancement factor of $\gamma \approx 100-150$, and consequently a local electric field of ∼10 MV/cm. These field strengths can be comparable to those required for field desorption of molecular ions from metal surfaces, which are in the order of 10−100 MV/cm [39,40]. However, we do not observe ions at the MCP without the laser pulses, even at constant field strength of up to 65 MV/cm.

As shown in Fig. 2(b), the MCP pulse rate exhibits a nonlinear dependence on laser pulse energy, similar to the nonlinear response observed in other strong-field phenomena such as photoemission from metallic nanotips [23,24]. In contrast, the peak FWHM remains nearly constant. This indicates that increasing optical fluence enhances the probability of laser-stimulated desorption without substantially altering the observed temporal characteristics of the emitted ions. The nearly invariant FWHM suggests that the measured pulse duration is primarily determined by the ion acceleration dynamics and the electronic timing response, rather than by thermal broadening or space-charge effects. At higher pulse energies, the pulse rate approaches a saturation regime, which can be attributed to the finite number of adsorbed species available on the tip surface between successive laser pulses. Once the local adsorbate coverage is depleted, further increases in laser energy do not lead to additional ion emission. This saturation behavior supports the interpretation that the process is surface-limited rather than intensity-limited under the present conditions.

The strong dependence of the MCP pulse rate on the laser polarization, as shown in Fig. 2(c), confirms that the ionization process involves field-enhanced photoemission at the nanotip apex. Maximum yield is obtained when the laser electric field is aligned with the tip axis ($\theta = 0^\circ$ or 180°), where the local field enhancement at the apex is strongest. As the polarization is rotated toward $\theta = 90^\circ$, the effective field enhancement at the apex decreases, leading to a rapid reduction in ion pulse rate. At these angles, a slight increase in the measured FWHM is observed. This broadening is partly due to the significantly lower count rate, which increases the statistical uncertainty of the width determination. It may also indicate the contributions from off-axis emission sites with less favorable field geometry and longer ion trajectories. Also, these off-axis ions are likely deflected onto the drift tubes and therefore do not contribute to the detected signal. Polarization-dependent behavior of laser-induced desorption has been reported previously [19,41].

As illustrated in Fig. 2(d), at low repetition rates, the MCP count rate increases linearly with laser repetition rate. This indicates that, for sufficiently high pressures or higher repetition rates, the emission probability per pulse can approach unity, leading to ion fluxes that scale proportionally with the laser repetition rate. At the maximum pressures used here, the detected ion rate reaches $\sim 10^3$ ions/s at a laser repetition rate of 1 kHz. However, at higher laser repetition rates and lower gas pressures, this trend begins to saturate and eventually plateaus, as the adsorbate replenishment on the tip surface becomes rate limiting. This plateau can be attributed to the depletion of adsorbates between successive laser pulses. At high repetition rates, there may be insufficient time between two consecutive laser pulses for gas molecules to adsorb and sustain a stable density at the tip, especially under low-pressure conditions. In particular, this plateau is proportional to the working gas pressure, as the Hertz-Knudsen equation [42] implies. This supports the idea that, in the case of high repetition rates, the process is adsorbate limited. Applying the Langmuir adsorption model [43] together with the sticking coefficient of H_2 on tungsten (∼0.32 [44]), we determine that the adsorbate density does not exceed $\sim 0.02\,\mathrm{nm}^{-2}$ once the pulse rate diverges from the laser repetition rate. Consequently, we find a surface-catalyzed ionization cross section of $\sim 50\,\mathrm{nm}^2$ ($= 5 \times 10^{-13}\,\mathrm{cm}^2$), which is approximately 4 orders of magnitude larger than the one for single-photon ionization in the gas phase at similar wavelengths [45,46] and about 3 orders of magnitude larger than the peak electron impact ionization cross section [47].

Interestingly, we observe no significant change in the pulse width of the ions as a function of the repetition rate. This indicates that pulse broadening is not influenced by thermally driven tip dynamics, as higher repetition rates result in increased energy deposition, and thus greater average heating at the tip.

Figure 3 shows a linear relation between the partial pressure and the MCP count rate for deuterium and nitrogen ions, also indicating that the production of ions is surface limited and depends on the availability of the adsorbates. Hydrogen, deuterium, carbon, nitrogen, and oxygen readily chemisorb onto tungsten [48–51] and may dissociate into atomic species on its surface [44]. In contrast, noble gases such as helium, argon, and krypton produce no detectable MCP signals at any tested pressure. This is consistent with their weak physisorption on tungsten surfaces, particularly at room temperature, where our experiments were performed [30,31,52].

Direct laser-induced ionization from the gas phase can be excluded in our case, as the ionization energies of argon (15.8 eV) and krypton (14.0 eV) are comparable to those of molecular hydrogen (15.4 eV) and nitrogen (15.6 eV), respectively [53]. If gas-phase ionization were to occur, one would expect to observe ionization from all these species under similar conditions. Moreover, the photon energy of the UV laser employed is 4.8 eV, which is significantly below the ionization threshold of these gases. Consequently, direct single-photon ionization is energetically forbidden, and multiphoton absorption processes would be required, which are improbable for our low laser fluences [54].

As demonstrated in Fig. 4, increasing the tip potential reduces both the mean TOF and the peak width. This shortening in time is due to stronger acceleration gradients near the emission point, which minimize the impact of the initial energy and position spread. The influence of the drift tube potentials is more subtle. Although changes in focusing DT_f have a limited influence on the pulse width, varying the extraction DT_e significantly alters the peak shape. This sensitivity arises because DT_e regulates the initial postemission acceleration zone, similar to the tip potential, in which the ions are still low energetic. Here, variations in kinetic energy and acceleration have the largest effect on the TOF dispersion. In contrast, DT_f

primarily collimates and focuses ions that have already been accelerated and has a more limited impact on ion timing.

The SIMION simulations reproduce the experimentally observed mean TOF values across different ion species, supporting our spectral peak assignments (cf. Fig. 4). The chosen grid spacing of 0.05 mm introduces in regions of steep field gradients, such as near the tip apex, TOF variations of $\sim$100−500 ps over the total trajectory length of 20.7 mm. Although a finer or adaptive grid could improve spatial resolution [55], the present simulations were designed primarily to confirm relative TOF trends rather than to model the ultrafast pulse profiles in quantitative detail. Within this intended scope, the excellent agreement between simulated and experimental mean TOFs demonstrates that the level of spatial resolution is adequate for reliable species identification.

In our setup, the ion detection is based on MCP signals, which are triggered upon the arrival of ions at the detector. As the total ion flux and transmission efficiency of our setup cannot be measured directly, the yield analysis is based on detected MCP pulse counts, which define the ion detection rate used throughout this work. Additionally, the MCP detector cannot distinguish between simultaneous impacts, as they will be combined in one output voltage pulse. Simulations suggest that multiple ions have to be emitted from the nanotip per laser pulse to have at least one ion reaching the detector. This has to particularly hold true for lower repetition rates, as each laser pulse yields an ion-triggered MCP signal. While a careful pulse height analysis on the MCP indicates laser parameter regimes with significantly more than one ion per laser pulse, it is currently not possible to reliably quantify the ion population per pulse. Yet, at repetition rates of several kHz (or more at higher loading pressures) with possibly $\gg$1 ion per pulse, the source efficiency is well comparable to typical laser and electron pump-probe experiments.

V. CONCLUSION AND OUTLOOK

We have demonstrated a method for generating ultrashort ion pulses with sub-100 ps duration through laser-stimulated desorption from a tungsten nanotip at room temperature. Using the localized field enhancement at the apex of an electrochemically etched metallic tip, we achieved temporal control over the ion emission with a moderate UV laser fluence of $\sim 10^{11}$ W/cm^2. This avoids the need for high-power femtosecond laser systems, which are usually required for these timing resolutions. The resulting ion pulses were characterized using a TOF technique, featuring sharp temporal profiles and high reproducibility.

Our approach introduces a compact and tunable ion source with a working principle at the intersection of ultrafast optics, nanoscale field emission, and surface science. The observed ion yields exhibit a strong dependence on laser polarization and gas pressure, confirming the role of field enhancement, surface adsorption, and molecular dissociation at the surface in the ionization process. TOF spectra and corresponding simulations show that the peak position shifts consistently with the applied potentials, validating the species identification.

Looking ahead, a nanometric ionization volume not only enables ion pulses short in time, but is the inherent requirement to facilitate high spatial resolution of a pulsed ion beam as well. Under the present conditions, ion count rates of up to 10^3 ions/s at 1 kHz repetition rate were obtained. For higher gas pressures or repetition rates, the flux can be expected to scale proportionally, ultimately allowing efficient ($\geqslant$kHz) production of picosecond ion pulses with $\gtrsim$1 ion/pulse in a future focused ion beam scheme. With both spatial and temporal control, high count rates, free choice of ion species, and sharp energy distribution for keV ions, true time-resolved ion scattering experiments are now in reach.

Finally, integrating cryogenic cooling or alternative tip materials could stabilize the replenishment of adsorbates through a higher sticking coefficient and more efficient catalytic molecular dissociation and ionization. It may also expand the accessible range of ion species toward noble gases [56]. Moreover, a pump-probe experiment could be realized by placing a sample at the current MCP position and introducing a controlled delay to the same laser pulse that triggers the ion emission, such that one pulse acts as the pump and the other as the probe, with variable delay between them. Our work thus builds the foundation for pump-probe experiments and ultrafast ion-surface dynamic studies.

ACKNOWLEDGMENT

This research was funded in whole or in part by the Austrian Science Fund (FWF) [10.55776/Y1174].

DATA AVAILABILITY

The data that support the findings of this article are openly available [57].

[1] G. Dearnaley, Ion implantation, Nature (London) **256**, 701 (1975).

[2] M. A. Hughes, Y. Fedorenko, B. Gholipour, J. Yao, T.-H. Lee, R. M. Gwilliam, K. P. Homewood, S. Hinder, D. W. Hewak, S. R. Elliott, and R. J. Curry, N-type chalcogenides by ion implantation, Nat. Commun. **5**, 5346 (2014).

[3] J. van Donkelaar, C. Yang, A. D. C. Alves, J. C. McCallum, C. Hougaard, B. C. Johnson, F. E. Hudson, A. S. Dzurak, A. Morello, D. Spemann, and D. N. Jamieson, Single atom devices by ion implantation, J. Phys.: Condens. Matter **27**, 154204 (2015).

[4] M. N. Bui, S. Rost, M. Auge, J.-S. Tu, L. Zhou, I. Aguilera, S. Blügel, M. Ghorbani-Asl, A. V. Krasheninnikov, A. Hashemi, H.-P. Komsa, L. Jin, L. Kibkalo, E. N. O'Connell, Q. M. Ramasse, U. Bangert, H. C. Hofsäss, D. Grützmacher, and B. E. Kardynal, Low-energy Se ion implantation in MoS_2 monolayers, npj 2D Mater. Appl. **6**, 42 (2022).

[5] B. Schmidt and K. Wetzig, *Ion Beams in Materials Processing and Analysis* (Springer, Vienna, 2013).

[6] S. Kretschmer and A.V. Krasheninnikov, Atomistic simulations of low energy ion irradiation of 2D materials: From *ab-initio* molecular dynamics to simple binary collision model, Phys. Rev. Mater. **8**, 114003 (2024).

[7] K. Nordlund, Historical review of computer simulation of radiation effects in materials, J. Nucl. Mater. **520**, 273 (2019).

[8] M. C. Fischer, J. W. Wilson, F. E. Robles, and W. S. Warren, Invited review article: Pump-probe microscopy, Rev. Sci. Instrum. **87**, 031101 (2016).

[9] A. Duvenbeck, B. Weidtmann, and A. Wucher, Predicting kinetic electron emission in molecular dynamics simulations of sputtering, J. Phys. Chem. C **114**, 5715 (2010).

[10] A. Wucher and A. Duvenbeck, Kinetic excitation of metallic solids: Progress towards a microscopic model, Nucl. Instrum. Methods Phys. Res. Sect. B **269**, 1655 (2011).

[11] P. Kung, H.-c. Lihn, H. Wiedemann, and D. Bocek, Generation and measurement of 50-fs (rms) electron pulses, Phys. Rev. Lett. **73**, 967 (1994).

[12] H. Niikura, F. Légaré, R. Hasbani, A. D. Bandrauk, M. Y. Ivanov, D. M. Villeneuve, and P. B. Corkum, Sub-laser-cycle electron pulses for probing molecular dynamics, Nature (London) **417**, 917 (2002).

[13] C. Höhr, D. Fischer, R. Moshammer, A. Dorn, and J. Ullrich, A subnanosecond pulsed ion source for micrometer focused ion beams, Rev. Sci. Instrum. **79**, 053102 (2008).

[14] B. Dromey, M. Coughlan, L. Senje, M. Taylor, S. Kuschel, B. Villagomez-Bernabe, R. Stefanuik, G. Nersisyan, L. Stella, J. Kohanoff, M. Borghesi, F. Currell, D. Riley, D. Jung, C.-G. Wahlström, C. Lewis, and M. Zepf, Picosecond metrology of laser-driven proton bursts, Nat. Commun. **7**, 10642 (2016).

[15] L. Kalkhoff, A. Golombek, M. Schleberger, K. Sokolowski-Tinten, A. Wucher, and L. Breuer, Path to ion-based pump-probe experiments: Generation of 18 picosecond KeV Ne ion pulses from a cooled supersonic gas beam, Phys. Rev. Res. **5**, 033106 (2023).

[16] A. Golombek, L. Danzig, and A. Wucher, Characterization of a supersonic gas jet via laser-induced photoelectron ionization, Nucl. Instrum. Methods Phys. Res. Sect. B **480**, 1 (2020).

[17] E. Ntemou, R. Holeňák, D. Wessman, and D. Primetzhofer, Picosecond pulsed beams of light and heavy keV ions at the time-of-flight medium energy ion scattering system at Uppsala University, Nucl. Instrum. Methods Phys. Res. Sect. B **556**, 165494 (2024).

[18] M. C. C. Mihaila, G. L. Szabo, A. Redl, M. Goldberger, A. Niggas, and R. A. Wilhelm, Generation of ultrashort ion pulses from ultrafast electron-stimulated desorption, Phys. Rev. Res. **6**, L032066 (2024).

[19] R. F. Haglund, Mechanisms of laser-induced desorption and ablation, in *Laser Ablation and Desorption*, edited by J. C. Miller and R.F. Haglund (Academic Press, Nashville, Tennessee, 1997), Vol. 30, pp. 15–138.

[20] B. Gault, A. Chiaramonti, O. Cojocaru-Mirédin, P. Stender, R. Dubosq, C. Freysoldt, S. K. Makineni, T. Li, M. Moody, and J. M. Cairney, Atom probe tomography, Nat. Rev. Methods Prim. **1**, 51 (2021).

[21] D. A. Cremers and L. J. Radziemski, *Handbook of Laser-Induced Breakdown Spectroscopy* (John Wiley & Sons Ltd, England, 2006).

[22] A.W. Miziolek, V. Palleschi, and I. Schechter, *Laser-Induced Breakdown Spectroscopy (LIBS)* (Cambridge University Press, New York, 2006).

[23] M. Krüger, M. Schenk, and P. Hommelhoff, Attosecond control of electrons emitted from a nanoscale metal tip, Nature (London) **475**, 78 (2011).

[24] P. Hommelhoff, Y. Sortais, A. Aghajani-Talesh, and M. A. Kasevich, Field emission tip as a nanometer source of free electron femtosecond pulses, Phys. Rev. Lett. **96**, 077401 (2006).

[25] H. Yanagisawa, T. Greber, C. Hafner, and J. Osterwalder, Laser-induced field emission from a tungsten nanotip by circularly polarized femtosecond laser pulses, Phys. Rev. B **101**, 045406 (2020).

[26] L. Bartolini, A. Poletti, R. Marks, E. Verlato, F. Paolucci, S. Rapino, and C. Albonetti, Revised electrochemical etching system for a reproducible fabrication of ultra-sharp tungsten tips, J. Appl. Electrochem. **51**, 551 (2021).

[27] Monaco 1035 Datasheet, Coherent Corp. (2023), accessed 17 April 2025.

[28] L.-H. Hong, B.-Q. Chen, C.-Y. Hu, and Z.-Y. Li, Spatial–temporal evolution of ultrashort laser pulse second Harmonic generation in β-barium borate (β-BBO) crystal, J. Appl. Phys. **129**, 233102 (2021).

[29] D. J. Manura and D. A. Dahl, SIMION Software Package, Version 8.1 (2014).

[30] T. Engel and R. Gomer, Adsorption of inert gases on tungsten: Measurements on single crystal planes, J. Chem. Phys. **52**, 5572 (1970).

[31] D. Nguyen-Manh and S. Dudarev, Trapping of he clusters by inert-gas impurities in tungsten: First-principles predictions and experimental validation, Nucl. Instrum. Methods Phys. Res. Sect. B **352**, 86 (2015).

[32] J. Byskov-Nielsen, J.-M. Savolainen, M. S. Christensen, and P. Balling, Ultra-short pulse laser ablation of metals: Threshold fluence, incubation coefficient and ablation rates, Appl. Phys. A **101**, 97 (2010).

[33] T. Genieys, M. Sentis, and O. Utéza, Measurement of ultrashort laser ablation of four metals (Al, Cu, Ni, W) in the single-pulse regime, Adv. Opt. Technol. **9**, 131 (2020).

[34] S. Mittelmann, J. Riedlinger, B. Buchner, T. Schwarz-Selinger, M. Mayer, and G. Pretzler, Ablation characteristics of tungsten with ultra-short laser pulses, J. Appl. Phys. **136**, 103103 (2024).

[35] J. Byskov-Nielsen, J.-M. Savolainen, M. S. Christensen, and P. Balling, Ultra-short pulse laser ablation of copper, silver and tungsten: Experimental data and two-temperature model simulations, Appl. Phys. A **103**, 447 (2011).

[36] P. Lickschat, D. Metzner, and S. Weißmantel, Fundamental investigations of ultrashort pulsed laser ablation on stainless steel and cemented tungsten carbide, Int. J. Adv. Manuf. Technol. **109**, 1167 (2020).

[37] T. T. Tsong and T. J. Kinkus, Energy distributions of pulsed-laser field-desorbed gaseous ions and field-evaporated metal ions: A direct time-of-flight measurement, Phys. Rev. B **29**, 529 (1984).

[38] D. Biswas, A universal formula for the field enhancement factor, Phys. Plasmas **25**, 043113 (2018).

[39] D. J. Harvey, Mass spectrometric detectors for gas chromatography, in *Gas Chromatography*, *Handbooks in Separation Science*, edited by C.F. Poole, 2nd ed. (Academic Press, Amsterdam, 2021), Chapter 14, pp. 399–424.

[40] S. E. Egorov, V. S. Letokhov, and E. V. Moskovets, Laser-stimulated field desorption of molecular ions from a tungsten emitter, Appl. Phys. B **45**, 53 (1988).

[41] H. Zacharias, G. Eichhorn, R. Schliesing, and K. Al-Shamery, Polarization dependence in the UV laser desorption of NO from NiO (100), Appl. Phys. B: Lasers Opt. **68**, 605 (1999).

[42] K.W. Kolasinski, *Surface Science* (John Wiley & Sons Ltd, United Kingdom, 2012).

[43] I. Langmuir, The adsorption of gases on plane surfaces of glass, MICA and platinum, J. Am. Chem. Soc. **40**, 1361 (1918).

[44] A. Rodríguez-Fernández, L. Bonnet, P. Larrégaray, and R. D. Muiño, *Ab initio* molecular dynamics of hydrogen on tungsten surfaces, Phys. Chem. Chem. Phys. **23**, 7919 (2021).

[45] J. J. Yeh, *Atomic Calculation of Photoionization Cross-sections and Asymmetry Parameters* (Gordon and Breach Science Publishers, Langhorne, PE, USA, 1993).

[46] J. J. Yeh and I. Lindau, Atomic subshell photoionization cross sections and asymmetry parameters: $1 \leqq Z \leqq 103$, At. Data Nucl. Data Tables **32**, 1 (1985).

[47] K. Irikura, Electron-impact cross section for ionization and excitation, NIST Standard Reference Database 107 (1997), doi: 10.18434/T4KK5C.

[48] P. J. Estrup and J. Anderson, Chemisorption of hydrogen on tungsten (100), J. Chem. Phys. **45**, 2254 (1966).

[49] H. F. Busnengo and A. E. Martínez, H_2 chemisorption on W(100) and W(110) surfaces, J. Phys. Chem. C **112**, 5579 (2008).

[50] J.K. Roberts, Adsorption of nitrogen on tungsten, Nature (London) **137**, 659 (1936).

[51] A. Mazumdar and H.-W. Wassmuth, Mass-spectrometric study of the chemisorption of oxygen on tungsten under transient and steady-state desorption conditions, Surf. Sci. **30**, 617 (1972).

[52] E. Zaremba and W. Kohn, Theory of helium adsorption on simple and noble-metal surfaces, Phys. Rev. B **15**, 1769 (1977).

[53] P. Linstrom and W. Mallard, NIST chemistry webbook (standard reference database number 69) (2025), doi: 10.18434/T4D303.

[54] R.W. Boyd, *Nonlinear Optics*, 4th ed. (Elsevier, United Kingdom, 2020).

[55] C. Oberdorfer, S. M. Eich, and G. Schmitz, A full-scale simulation approach for atom probe tomography, Ultramicroscopy **128**, 55 (2013).

[56] G. Hlawacek, V. Veligura, R. van Gastel, and B. Poelsema, Helium Ion microscopy, J. Vac. Sci. Technol. B **32**, 020801 (2014).

[57] A. Redl, M. Goldberger, C. Pachlinger, F. Pfanner, and R. A. Wilhelm, Generation of Picosecond Ion Pulses Using Laser-Stimulated Desorption from a Tungsten Nanotip - Dataset [Data set], TU Wien, (2025), https://doi.org/10.48436/71sdw-ezf55.